Catalytic high-temperature conversion of renewable syngas to methane

D.A Rodríguez-Pastor*[*,a], S. Guadix-Gil[b], A. Carro[c], V.M. Soltero[d], R. Chacartegui[e]

[a] *University of Seville, Escuela Técnica Superior de Ingenieros, Camino de los Descubrimientos s/n, 41092 Seville, Spain, drodriguez4@us.es*

[b] *University of Seville, Escuela Técnica Superior de Ingenieros, Camino de los Descubrimientos s/n, 41092 Seville, Spain, sguadix@us.es*

[c] *Departamento de Ingeniería, Universidad Loyola Andalucía, Spain, acarro@uloyola.es*

[d] *University of Seville, Escuela Politécnica Superior, 41011, Seville, Spain, vmsoltero@us.es*

[e] *University of Seville, Escuela Técnica Superior de Ingenieros, Camino de los Descubrimientos s/n, 41092 Seville, Spain, ricardoch@us.es*

Abstract:

Seasonal storage of renewable electricity requires chemical carriers that are compatible with existing gas networks. The methanol-to-methane thermochemical cycle meets this requirement, but its methanation stage, which is exothermic, prone to hotspots and has a net heat demand, constitutes the unresolved bottleneck for industrial deployment. This work presents a one-dimensional pseudo-homogeneous piston-flow model for a fixed-bed methanation reactor comprising three adiabatic stages, with Langmuir-Hinshelwood-Hougen-Watson kinetics based on Ni catalysts, interstage steam generation and pinch analysis, varying the spatial time τ_W across industrial ranges. CO conversion increases from 83.1% to 93.1% as τ_W increases, whilst the maximum temperature drops from 541°C (nine degrees below the sintering threshold) to a stable plateau of 493°C, redistributing the axial heat release from a concentrated hotspot to a spatially extended profile better suited to thermal integration. The third stage of the reactor accounts for over 60% of the total reaction enthalpy and governs steam generation capacity. The value of τ_W = 200 $kg_{cat} \cdot s \cdot mol^{-1} H_2$ strikes a balanced compromise among conversion, catalytic integrity and energy integration. Dynamic operation under variable renewable input constitutes the decisive open challenge for grid-scale deployment.

Keywords:

Methanation; Renewable Syngas; Kinetics; Hydrogen; SNG.

1. Introduction

The decarbonization of industrial energy use and power systems with shares of variable renewable electricity requires energy carriers that can complement direct electrification through large-scale storage, transportability, and compatibility with existing infrastructure [1,2]. Within this context, synthetic natural gas (SNG) occupies a distinctive position because methane can be stored and distributed through the established natural-gas network [3], while gas storage and power-conversion technologies based on natural gas are already commercially mature [4]. For this reason, methanation-based routes are increasingly viewed as a bridge between fluctuating renewable power [5], chemical energy storage [6], and the progressive decarbonisation of sectors that remain structurally dependent on gaseous fuels [7].

That rationale becomes even more compelling when methane is produced not only from captured CO_2 and electrolytic hydrogen, but also from renewable synthesis gas streams already rich in CO and H_2 [8]. Such syngas can be generated from biomass gasification [9], from the co-electrolysis of CO_2 and H_2O [10], or from other renewable synthesis schemes in which the H_2/CO ratio is adjusted upstream of methanation to meet downstream conversion targets [11]. Renewable syngas methanation addresses feedstocks in which carbon is distributed between CO and CO_2, hydrogen availability is composition-dependent, and upstream conditioning strongly influences both reactor feasibility and carbon utilisation [12].

From a reaction standpoint, three cases must therefore be clearly distinguished. CO methanation, which refers to the direct hydrogenation of CO-rich mixtures, has historically underpinned SNG production from synthesis gas [13]. CO_2 methanation is the Sabatier route based on CO_2/H_2 feeds and dominates a large fraction of the current Power-to-Gas literature [14]. Methane formation proceeds in a reactive environment where CO conversion, CO_2 redistribution, and water-gas-shift-related effects can all influence the local driving force and product composition [15]. In a CO-rich renewable syngas service, the process must therefore balance strong

exothermicity [16], equilibrium limitations at elevated temperature and hot-spot formation [17] and the catalyst risks of sintering or poisoning [18]. Industrial and preindustrial SNG concepts have mainly evolved along two broad lines: multistage adiabatic fixed-bed trains with interstage cooling and alternative reactor concepts with enhanced heat removal and fluidised beds have been developed to mitigate temperature peaks and expand the operability window [19]. Multibed adiabatic fixed beds are sustained by their practical simplicity, scalability, and industrial familiarity [20], but it also means that conversion, thermal management, and catalyst utilisation are inseparable from the design of interstage cooling [21]. When intermediate cooling is implemented using steam raisers, it enables the recovery of reaction heat as useful steam, thereby improving heat management [22]. This point is important for renewable syngas schemes because variations in feed composition and methane specification propagate directly into stage inlet temperatures, cooling duties, and the amount of recoverable thermal energy.

These interactions simultaneously involve kinetics, equilibrium, transport phenomena, and energy integration. Overall, modelling is crucial for reducing the design space before pilot validation. Comparative reactor-modelling studies have shown that a one-dimensional pseudo-homogeneous representation can already provide predictions of conversion and maximum temperature for preliminary design purposes [23], even though more detailed heterogeneous or multidimensional descriptions become necessary when pellet-scale transport, external heat transfer, or highly structured geometries govern the response [24]. For multistage adiabatic fixed-bed methanation, this compromise is valuable because key questions concern stage-wise temperature rise, sensitivity to feed composition, catalyst allocation, and exchanger duty rather than a full resolution of radial gradients at every axial coordinate [25]. Most of the recent reactor works are centred on CO_2 methanation [26], while syngas-oriented studies often focus on catalyst comparison [27], single-reactor behaviour [28], or broader flowsheet demonstrations without fully resolving the coupled effects of CO methanation, WGS-related chemistry, and heat recovery in staged adiabatic operation.

Against this background, a specific research gap emerges between the maturity of general methanation knowledge and the needs of the renewable syngas-to-SNG process design. Although the literature provides robust foundations in methanation chemistry, classical industrial configurations, and reactor modelling, comparatively few studies examine CO-rich renewable syngas in multistage adiabatic fixed-bed reactors through a framework that is at once composition-sensitive, reactor-design oriented, and explicit about thermal integration via steam generation. This omission matters because a reactor train that appears satisfactory in terms of carbon conversion may still be thermally suboptimal or operationally misleading once stage temperature constraints and interstage steam recovery are considered together. The present work addresses this gap by developing a one-dimensional model for the catalytic methanation of CO-rich renewable syngas in three adiabatic fixed-bed reactors in series, including at least CO methanation and WGS, with interstage cooling through steam raisers and an explicit emphasis on both reactor behaviour and thermal integration. This work seeks to clarify how syngas composition controls thermal response, equilibrium approach, and stage utilisation, and to provide a rigorous basis for simulation, sensitivity analysis, and preliminary optimisation of SNG production from renewable synthesis gas.

2. High temperature CO methanation

High-temperature CO methanation refers to the operating range between 450 °C and 700 °C [29], thus differing from the low-temperature regime (<400 °C) where thermodynamics favour high conversion rates [26], but the intrinsic kinetics are insufficient without particularly active catalysts. In the context of synthetic natural gas (SNG) production from renewable CO, derived from biomass gasification, CO2 electrolysis (reverse water-gas shift, RWGS) or direct air capture (DAC) processes, the high-temperature regime is particularly significant because the synthesis gas obtained in these processes typically emerges at temperatures between 500 °C and 900 °C [30], allowing for direct thermal integration with the methanation reactor without the need for prior cooling, thereby improving the overall energy balance of the process [31]. The central reaction is the same as in the low-temperature regime and is shown in Eq. 1:

$$CO + 3H_2 \rightarrow CH_4 + H_2O \qquad \Delta H^{\circ}_{298} = -206.2\ kJ\ mol^{-1} \tag{1}$$

using the coupled WGS reaction (Eq. 2):

$$CO + H_2O \rightarrow CO_2 + H_2 \qquad \Delta H^{\circ}_{298} = -41.2\ kJ\ mol^{-1} \tag{2}$$

Managing reaction heat becomes the primary challenge [32], as at high temperatures the heat generated per mole of CO converted is slightly lower due to the variation in $\Delta H_{r1}(T)$ with temperature, but the risk of localised overheating on the catalytic bed is increased due to the higher reaction rate [33], which releases heat in a more concentrated manner in the reactor inlet zone. At 500 °C, this equation implies an equilibrium favouring the products at moderate pressures. However, at 650 °C ($\ln K_{eq,1} < 1$), the maximum achievable conversion at 1 bar falls below 40–50% for stoichiometric mixtures [34]. This behaviour, therefore, necessitates that operation in the high-temperature regime must be carried out at high pressures (>10 bar) to thermodynamically

compensate for the unfavourable effect of temperature [35], or else implement series reactor configurations with intermediate cooling that maintain the local temperature within a kinetic-thermodynamic compromise window. The effect of pressure is particularly pronounced in the 500–700 °C range, industrial methanation processes typically operate between 20 and 60 bar when the aim is to maximise conversion in a single stage [36]. Furthermore, an excess of H2 relative to stoichiometry (H2/CO ratio between 3.5 and 5) shifts the equilibrium towards the products and simultaneously reduces the tendency for carbon deposition [37].

2.1. Catalysts for renewable CO methanation

Renewable CO derived from biomass gasification or RWGS processes has compositional characteristics that influence catalyst selection differently from fossil-derived synthesis gas. In particular, (i) the H_2S content may be lower than that of coal gases but is still significant (1–50 ppm) for solid waste gasification gases [38]; (ii) the presence of traces of chlorinated or alkaline compounds from the biomass may interact with the catalytic support [39]; and (iii) the intrinsic compositional variability of renewable sources requires catalysts with greater tolerance to H_2/CO ratio transients [40]. At high temperatures, additional requirements for the catalyst include thermal stability of the active phase and support, resistance to metal sintering (critical >600 °C) and the ability to operate in start-stop cycles without irreversible loss of activity [34], an operational requirement specific to Power-to-Gas systems coupled with intermittent renewable energy sources.

2.1.1. Ni-based catalytic systems

Ni supported on Al_2O_3, $MgAl_2O_4$, or mixed supports remains the industry standard for high-temperature CO methanation [41], for the reasons of cost and availability already discussed. At high temperatures, the stability of the support against phase transformation is critical, as γ-Al_2O_3 undergoes progressive phase transitions above 800–900 °C in the presence of water vapour, leading to a collapse in BET surface area and a loss of metal dispersion [42]. The addition of stabilisers such as La_2O_3, CeO_2 or MgO inhibits these transformations and maintains Ni dispersion at high operating temperatures [43]. The optimal Ni loading for high-temperature CO methanation lies in the range of 15–30 wt% NiO relative to the support [44], a value higher than that typically used in methane reforming, but justified by the need to maintain sufficient active site density when sintering progressively reduces dispersion during high-temperature operation. Catalyst reduction must be carried out at a sufficiently high temperature (> 500 °C in H_2) to ensure the complete reduction of NiO to Ni^0, a condition that is met in situ at high operating temperatures if the feed contains excess H_2 [45].

2.1.2. Modified promoters and supports

Doping with alkaline earth metals (Mg, Ca) improves the surface basicity of the catalyst [46], thereby reducing the dissociative adsorption of CO and the tendency for carbon deposition in the high-temperature regime, where the Boudouard reaction is kinetically accessible. Hu et al. [47] reported that the addition of 2-4 wt% MgO to Ni/Al_2O_3 significantly reduced the formation of carbon deposits at temperatures above 500 °C, whilst maintaining CH_4 selectivities above 95% with simulated renewable CO. The incorporation of CeO_2 as a promoter or support component has a dual effect in the proposed approach. On the one hand, it improves metal dispersion through Ce-Ni interaction, which stabilises small particles [48]; on the other hand, the Ce^{4+}/Ce^{3+} redox pair provides the capacity to store and mobilise surface oxygen, which facilitates the oxidation of carbonaceous intermediates and reduces the accumulation of C* on the active surface [49]. This mechanism is relevant when renewable CO comes from sources with stoichiometric variability, given that during periods of low H_2/CO ratio, CeO_2 can act as an additional oxygen reservoir to gasify the deposited carbon. Structured supports, such as SiC foams or cordierite monoliths coated with an Al_2O_3–Ni washcoat, have been proposed as an alternative to the conventional fixed bed [50]. The higher thermal conductivity of SiC allows for a more uniform temperature distribution, limiting local hot spots and extending the catalyst's useful life.

Table 1. Catalytic systems reported for the methanation of CO at high temperatures (> 450 °C) using renewable or biomass-derived CO

Metal	Support	Promoters	T (°C)	P (bar)	X_{CO}	S_{CH_4}	Reference
Ni	$MgAl_2O_4$	—	500–575	3–15	n.d.	n.d.	[51]
Ni	Al_2O_3	MgO (2–4%)	400–550	30	~100%	96.5%	[52]
Ni	Al_2O_3–CeO_2	Ce (5–15%)	450–650	10–30	> 90%	> 93%	[49]
Ni–Ru	Al_2O_3	Ru (0.5–2%)	400–600	5–20	> 95%	> 97%	[53]
Ni	SiC (foam)	—	500–700	20–50	> 85%	> 90%	[54]
Ni	Al_2O_3–La_2O_3	La (3–8%)	500–650	10–30	> 92%	> 95%	[53]

3. Methodology

The proposed process diagram (Figure 1) follows the architecture of the TREMP (Topsoe Recycle Energy-efficient Methanation Process) [55], in which three adiabatic reactors in series, with interstage recycling and high-pressure steam generation, constitute the industry-standard configuration for producing synthetic natural

gas from syngas. The syngas feed (H_2:CO = 2:1) is regulated in terms of flow rate and pressure by valve CV-101 and preheated in E-101 to the Ni catalyst activation temperature before entering the first fixed-bed adiabatic reactor, R-101. A fraction of the hot effluent from R-101 is recirculated via heat exchanger E-104 and its associated compressor to the inlet of the process train: this dilution reduces the concentration of fresh reactants and controls the adiabatic temperature rise in the first stage, where the higher kinetic load and high CO concentration increase the risk of exceeding the catalyst sintering threshold (~550°C).

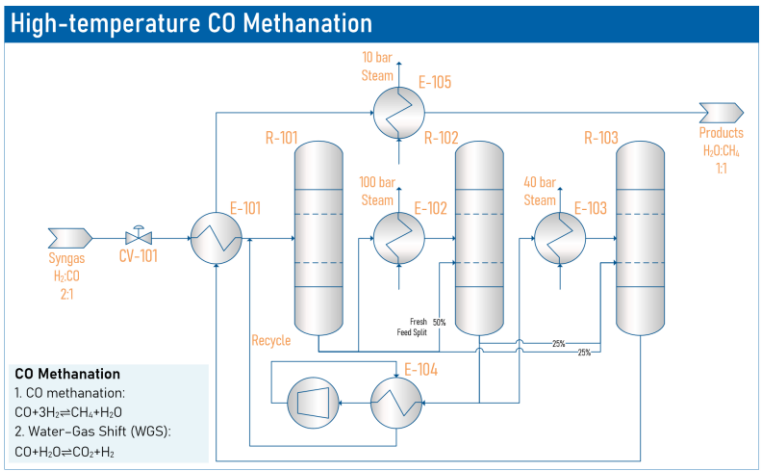

Figure 1. Process flow diagram of the high-temperature CO methanation system with three adiabatic fixed-bed reactors in series and interstage steam generators.

The effluent from R-101, which is still at a high temperature, is cooled in E-102 by generating saturated steam at 100 bar before entering R-102. This strategy recovers the reaction heat rather than dissipating it through a conventional heat exchanger, allowing up to 85% of the released reaction heat to be recovered as high-pressure steam. Between R-102 and R-103, steam is generated at 40 bar in E-103, and at the outlet of R-103, steam at 10 bar is produced in E-105. The decreasing vapour pressure along the process train is a direct consequence of the progressively lower temperature of the reactor effluents as the conversion progresses towards equilibrium. The product stream at the outlet of R-103, with an H_2O:CH_4 ratio of ~1:1, requires a condensation and water-separation stage to meet the specification for a substitute natural gas suitable for injection into the grid.

3.1. System modelling

The proposed reaction system is modelled using a one-dimensional pseudo-homogeneous piston-flow reactor (PFR) for a catalytic fixed-bed reactor operated under steady-state conditions. In this approach, the gas and solid phases are treated as an effective continuum, and axial dispersion of mass and heat is neglected. The independent variable is the catalyst mass W [kg_{cat}], which allows the problem to be formulated independently of the reactor's geometric length. The state vector is defined as $\mathbf{y} = [F_{CO}, F_{H_2}, F_{CH_4}, F_{H_2O}, F_{CO_2}, T, P]^T$, where F_i [mol s^{-1}] is the molar flux of the species i, T [K] is the temperature of the gas and P [Pa] is the total pressure. The differential molar balance for each species with respect to W is written as Eq. 4:

$$\frac{dF_i}{dW} = \sum_{j=1}^{2} \nu_{ji}\, r_j \qquad i \in \{CO, H_2, CH_4, H_2O, CO_2\} \tag{4}$$

where ν_{ji} is the stoichiometric coefficient of the species i in the reaction j, positive for products and negative for reagents, and r_j [mol kg_{cat}^{-1} s^{-1}] is the net reaction rate j relating to the catalyst mass relating to the catalyst mass. For an adiabatic bed, the differential energy balance is expressed as Eq. 5:

$$\frac{dT}{dW} = -\frac{\sum_{j=1}^{2} r_j\ \Delta H_{r,j}(T)}{C_{p,\mathrm{tot}}(T)} \tag{5}$$

where $\Delta H_{r,j}(T)$ [J mol^{-1}] is the reaction enthalpy of the reaction j at the local temperature and $C_{p,\mathrm{tot}}(T)$ [J s^{-1} K^{-1}] is the total extensive heat capacity of the gas $C_{p,\mathrm{tot}}(T) = \sum_i F_i\ C_{p,i}(T)$. The pressure drop is calculated using Ergun's equation for flow in packed beds (Eq. 6):

$$-\frac{dP}{dz} = \frac{150\ \mu_g (1-\varepsilon_b)^2}{\varepsilon_b^3\ d_p^2}\ u + \frac{1.75\ \rho_g\ (1-\varepsilon_b)}{\varepsilon_b^3\ d_p}\ u^2 \tag{6}$$

where μ_g [Pa s] is the dynamic viscosity of the gas, ε_b is the void fraction of the bed, d_p [m] is the particle diameter, u [m s^{-1}] is the surface velocity (Eq. 7) and ρ_g [kg m^{-3}] is the density of the gas. Under ideal gas behaviour:

$$u = \frac{F_{\text{tot}} RT}{P\, A_r} \tag{7}$$

where A_r [m^2] is the cross-section of the reactor.

3.2. Reaction kinetics

The basic kinetic model adopted is that of Xu and Froment [56], formulated as a reversible Langmuir-Hinshelwood-Hougen-Watson model, applied consistently to both the methanation and WGS processes. The net reaction rates are expressed as Eq. 8-9:

$$r_1 = \frac{k_1(T)}{P_{H_2}^{2.5}} \frac{P_{CO} P_{H_2}^3 - \frac{P_{CH_4} P_{H_2O}}{K_{eq,1}(T)}}{DEN^2} \tag{8}$$

$$r_2 = \frac{k_2(T)}{P_{H_2}} \frac{P_{CO} P_{H_2O} - \frac{P_{CO_2} P_{H_2}}{K_{eq,2}(T)}}{DEN^2} \tag{9}$$

with the standard adsorption coefficient given by Eq. 10:

$$DEN = 1 + K_{CO}(T) P_{CO} + K_{H_2}(T) P_{H_2} + K_{CH_4}(T) P_{CH_4} + K_{H_2O}(T) \frac{P_{H_2O}}{P_{H_2}} \tag{10}$$

The values of the kinetic parameters are shown in Table A1. The equilibrium constants are calculated thermodynamically from the standard free energy of reaction (Eq. 11):

$$K_{eq,j}(T) = \exp\left(-\frac{\Delta G_{r,j}^{\circ}(T)}{RT}\right) \tag{11}$$

with $\Delta G_{r,j}^{\circ}(T)$ derived from JANAF/NIST data [57]. This formulation avoids inconsistencies between the kinetic and thermodynamic blocks.

3.3. Thermal integration

The process is configured using three adiabatic beds in series, separated by steam-generating heat exchangers. The fresh feed is distributed between stages via a vector $\mathbf{s} = [s_1, s_2, s_3]$ such that $\sum_k s_k = 1$. The flow entering the stage k is defined as $\mathbf{F}_{fresh}^{(k)} = [s_k F_{CO,0}, s_k F_{H_2,0}, 0, 0, 0]^T$, and is added to the cooled effluent from the previous stage before entering the next reactor. After each reactor, the process gas is cooled in a saturated steam generator. The target outlet temperature of the hot gas $T_{target}^{(k)}$ is set as $T_{target}^{(k)} = T_{sat}(P_{steam}^{(k)}) + \Delta T_{app}$ where ΔT_{app} is a design parameter for the approach temperature. The heat extracted in the heat exchanger k is given by the expression defined for Q_k, and the LMTD for an evaporator with an approximately isothermal cold side at T_{sat} is shown in Eq. 12:

$$LMTD_k = \frac{\left(T_{hot,in}^{(k)} - T_{sat}^{(k)}\right) - \left(T_{target}^{(k)} - T_{sat}^{(k)}\right)}{\ln\left[\frac{T_{hot,in}^{(k)} - T_{sat}^{(k)}}{T_{target}^{(k)} - T_{sat}^{(k)}}\right]} \tag{12}$$

The required area is obtained from the standard design equation $A_k = Q_k / U \cdot LMTD_k$ where U [W m^{-2} K^{-1}] is the overall heat transfer coefficient. The mass flow rate of the steam generated is calculated using the energy balance on the cold side, described in Eq. 13:

$$\dot{m}_{steam}^{(k)} = \frac{Q_k}{c_{p,L}\left(T_{sat}^{(k)} - T_{BFW}\right) + \Delta h_{vap}^{(k)}} \tag{13}$$

where $c_{p,L}$ [J kg^{-1} K^{-1}] is the heat capacity of liquid water, T_{BFW} [K] is the temperature of the feed water and $\Delta h_{vap}^{(k)}$ [J kg^{-1}] is the latent heat of vaporisation at the pressure of the vapour produced. Table 2 summarises the input parameters and operating conditions used in the simulation of the three-stage adiabatic methanation reactor. The process operates at 30 bars with a fresh feed inlet temperature of 330 °C, representative of industrial high-temperature methanation units. The catalyst mass is distributed across the three adiabatic stages in a 50/25/25% split, with a base-case spatial time of τ_W = 200 $kg_{cat} \cdot s \cdot mol^{-1}$ H_2. Bed hydrodynamics are described using the Ergun equation with the geometric and physical properties listed in Table 2.

Table 2. Operating conditions and input parameters for the proposed three-stage adiabatic methanation simulation

Parameter	Value
Inlet temperature	330 °C
Total operating pressure	30 bar
Molar flow rate of CO (fresh)	100 mol/s
Molar flow rate of H_2 (fresh)	200 mol/s
Catalyst fraction per stage	50 / 25 / 25 %
Spatial time (base case)	τ_W = 200 kg_{cat}·s·mol^{-1} H_2
Reactor diameter	3.0 m
Bed porosity	0.40
Catalyst density	1 200 kg/m^3
Pellet diameter	5 mm
Dynamic viscosity of the gas	2.5×10^{-5} Pa s

4. Results and discussion

Figure 2 illustrates the axial trend in CO conversion (ΔX_{CO}) through the three-stage adiabatic fixed-bed methanation reactor for τ_W = 200 kg_{cat}·s·mol^{-1} H_2, with a total cumulative length of approximately 12 m. In the first stage (0–4 m), ΔX_{CO} It starts from an initial value of 66%, resulting from a mixture of syngas with recycled product or from prior partial conversion during methanol decomposition [58], and it then rises sharply to values close to 92–93%. High inlet temperature favours the reaction rate, although the adiabatic temperature increase towards the interior of the bed shifts the thermodynamic equilibrium towards the reactants, limiting the maximum achievable conversion at each stage. In the second stage (4–7.5 m), ΔX_{CO} begins at ~40%, reflecting interstage cooling and the injection of fresh syngas, and then rises more gradually, showing a progressive approach to equilibrium at lower temperatures. In the third stage (7.5–12 m), CO conversion begins again at around 60% and reaches approximately 88–90% at the end of the reactor (less than 2% deviation compared to [54]), with a downward-sloping profile that demonstrates the kinetic inhibition exerted by the cumulatively generated water vapour and the proximity to thermodynamic equilibrium at moderate temperatures. This staged design with intermediate cooling is essential to resolve the trade-off between reaction rate and equilibrium conversion, overcoming the thermodynamic limitation that would otherwise prevent high conversions from being achieved in a single adiabatic reactor.

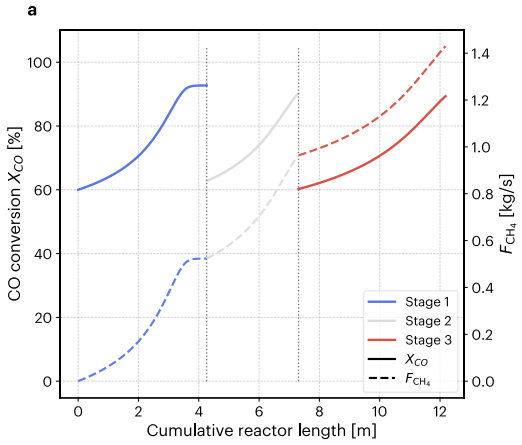

Figure 2. Axial profiles of CO conversion and methane production rate along the cumulative length of the three-stage adiabatic methanation reactor for the base case (τ_W = 200 kg·s·mol^{-1}).

The profile of methane production rates ($F_{C\,H_4}$, dashed lines) clearly illustrates the cumulative nature of the methanation process across the three stages. In the first stage, $F_{C\,H_4}$ rises to approximately 0.4 kg/s at the end of the first 4 m of the reactor, coinciding with the abrupt jump in ΔX_{CO} observed in that same section, confirming that most of the methane production in this stage occurs in a narrow axial zone where the kinetics are more favourable. In the second stage, cumulative production continues to increase, reaching around 0.8 kg/s at 7.5 m, with an intermediate rate of increase. It is in the third stage that the most significant absolute increase in $F_{C\,H_4}$ is recorded, rising from ~0.8 kg/s to ~1.4 kg/s in the final 4.5 m of the reactor, largely due to the greater available length and the conversion of residual CO fractions that did not react in the previous stages [59].

Figure 3 shows the axial temperature profiles in the three-stage adiabatic fixed-bed methanation system for four values of the modified spatial time τ_W, ranging from 100 to 250 kg·s·mol^{-1}. In all cases, the thermal profile

of each stage exhibits an initial low-slope zone where the reaction barely begins due to kinetic limitations at the feed temperature (~340°C), followed by a region of steep rise as the temperature increases and accelerates the reaction rate, and a final asymptotic zone where the approach to thermodynamic equilibrium progressively attenuates heat generation. This behaviour can be examined in more detail at [60]. Figure 3a (τ_W = 100 kg·s·mol⁻¹) records the highest maximum temperature in the series, T_{max} = 540.9°C, over a total length of 6.09 m. At high space velocities, the reactant flow rate is high per unit mass of catalyst, and the reaction releases heat within a very narrow axial zone, generating a sharp hotspot that approaches the thermal tolerance limit of Ni catalysts. As the τ_W increases to 150 kg·s·mol⁻¹ (Figure 3b), T_{max} drops to 478.6°C, as the lower kinetic load spreads the heat release over a greater reactor length (9.14 m), flattening the profile and reducing the temperature gradient. It is significant that for τ_W = 200 and 250 kg·s·mol⁻¹ (Figure 3c and 3d), T_{max} stabilises at 492.9 °C despite the additional increase in reactor length.

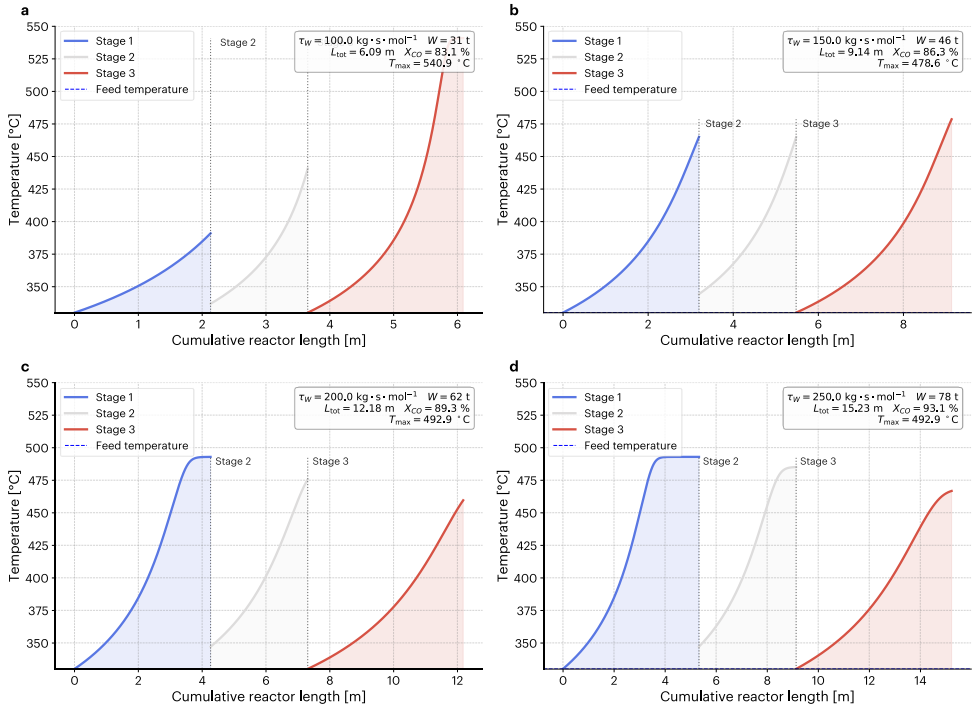

Figure 3. Axial temperature profiles in the three-stage adiabatic methanation reactor for four spatial steps (τ_W = 100, 150, 200 and 250 kg·s·mol⁻¹).

Figure 4 shows the hot and cold composite curves from the pinch analysis for the three-stage methanation system, evaluated at four spatial time values τ_W ranging from 100 to 250 kg·s·mol⁻¹, with a minimum approach temperature difference ΔT_{min} = 20 K. In all the panels, the hot composite curve, which combines the enthalpy contents of the reactor effluents and the high-temperature process gases, starts at a maximum temperature that decreases from ~560°C in Figure 4a to ~490°C in Figure 4c and 4d, in direct correlation with the reduction in T_{max} as rising τ_W [61]. The cold composite curve shows a steep section between ~300 and ~340°C, corresponding to the heat demand for vaporisation, whilst the gently sloping section below ~200°C reflects the preheating of liquid and gaseous streams with a higher accumulated heat capacity. The pinch point is at $Q \approx$ 18–20 MW and ~320–340°C in all panels, which constitutes the structural constraint of the heat exchange network. His position implies that no improvement in τ_W can significantly shift it. The overlap between the two curves in the interval $0 < Q < Q_{pinch}$ defines the maximum internally achievable heat recovery for each operating condition, without the need for external heat sources in that enthalpy region.

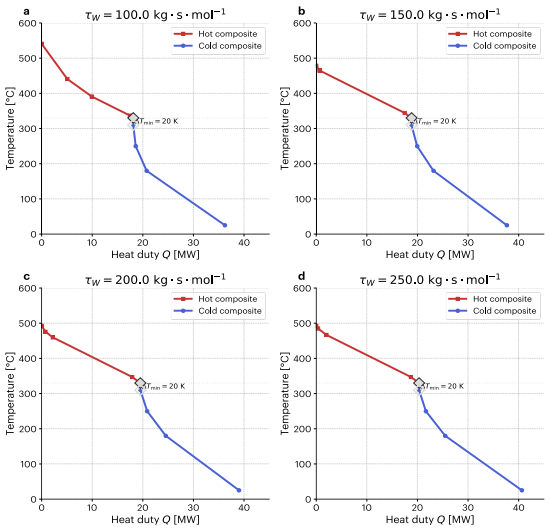

Figure 4. Hot and cold composite thermal integration curves from the pinch analysis for the system at four values of τ_W.

Figure 5 shows the grand composite curves (GCCs) for the methanation system at the four studied values of τ_W, represented as temperature versus the net heat available at each temperature level following the maximum internal recovery imposed by ΔT_{min} = 20 K. The morphology of the GCC makes it possible to determine directly, at each temperature level, how much energy can be transferred to external systems without violating the second law. Above the pinch, the four curves show a net heat flux that increases with temperature, reaching ~17.6 MW (τ_W = 100 kg·s·mol^{-1}) to ~20 MW (τ_W = 250 kg·s·mol^{-1}) at their respective maximum temperatures (~550°C and ~490°C), consistent with the higher total exothermic production of methane at higher spatial times. The point where the curves intersect with the horizontal reference lines for steam generation, plotted at the vapour saturation temperatures at 10 bar (~180°C), 40 bar (~250°C) and 100 bar (~311°C), defines the temperature thresholds at which it is thermodynamically feasible to generate steam at each pressure level using recovered process heat.

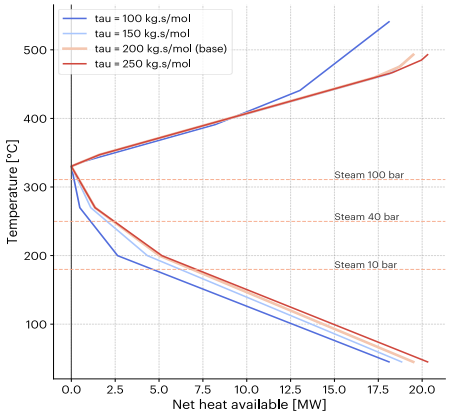

Figure 5. Net composite thermal integration curves of the methanation system for τ_W = 100–250 kg·s·mol^{-1}, showing the steam generation temperature levels at 10, 40 and 100 bar.

5. Conclusions

A one-dimensional pseudo-homogeneous plug flow model has been developed for a fixed-bed methanation reactor comprising three adiabatic stages in series, coupled with validated reaction kinetics and an integrated steam generation module incorporating pinch analysis (ΔT_{min} = 20 K), to characterise the process under varying catalyst load. The modified space-time τ_W proves to be the design variable with the greatest impact on the system; when the flow rate is increased from 100 to 250 kg·s·mol^{-1} H_2, CO conversion rises from 83.1% to 93.1%, whilst the maximum reactor temperature drops from 541°C to a stable plateau of 493°C, redistributing the axial heat release from an acute, concentrated hotspot towards a spatially extended profile that is more favourable for thermal integration. The third stage of the reactor accounts for over 60% of the total reaction enthalpy and determines the steam generation capacity (~6.4 MW at 100 bar, 2.56 kg/s), whilst pinch analysis reveals that the cooling demand structurally exceeds the exothermic output of methanation, imposing a net heat import that limits thermal efficiency regardless of the operating point. These results point to τ_W = 200 kg·s·mol^{-1} as a condition for balanced operation among conversion, catalyst thermal integrity and energy

integration, and identify dynamic operation under variable renewable input profiles as the key remaining challenge for the grid-scale deployment of syngas-based thermochemical storage systems.

Acknowledgments

This work has been partially funded by the project 'Renewable Methanol-based Synthetic Multifuel Production (METHCESFUEL)', from the European Commission through Horizon, the EU Framework Programme for Research and Innovation, under Grant Agreement No. 101235215.

Nomenclature

A_k	Heat transfer area of exchanger k, m²	K_{H_2O}	Adsorption equilibrium constant of H_2O, —
A_r	Reactor cross-sectional area, m²	k_j	Temperature rate constant, mol kg^{-1}cat s^{-1} bar^{-n}
C_{H_2}	Molar concentration, mol m^{-3}	$k_{j,0}$	Pre-exponential factor, mol kg^{-1}cat s^{-1} bar^{-n}
$C_{p,tot}$	Total extensive heat capacity, W K^{-1}	$LMTD_k$	Log-mean temperature difference k, K
$c_{p,i}$	Molar heat capacity, J mol^{-1} K^{-1}	$\dot{m}_{steam}$	Mass flow rate of generated steam, kg s^{-1}
$c_{p,L}$	Specific heat capacity of water, J kg^{-1} K^{-1}	P	Total pressure, Pa
D_{e,H_2}	Effective diffusivity of H_2, m² s^{-1}	P_i	Partial pressure of species i, bar
DEN	Adsorption denominator, —	P_{steam}	Steam generation pressure, bar
d_p	Pellet diameter, m	Q_k	Heat duty of exchanger k, W
$E_{a,j}$	Activation energy, J mol^{-1}	R	Universal gas constant, J mol^{-1} K^{-1}
F_i	Molar flow rate, mol s^{-1}	r_j	Reaction rate, mol kg^{-1}cat s^{-1}
F_{tot}	Total molar flow rate, mol s^{-1}	s_k	Feed split fraction, —
$\Delta G^\circ_{r,j}$	Gibbs energy, J mol^{-1}	T	Gas temperature, K
$\Delta H^\circ_{r,j}$	Enthalpy at 298 K, J mol^{-1}	T_{BFW}	Boiler feed water temperature, K
$\Delta H_{r,j}(T)$	Reaction enthalpy, J mol^{-1}	T_{max}	Maximum bed temperature, °C
Δh_{vap}	Latent heat, J kg^{-1}	T_{sat}	Saturation temperature, K
K_{CO}	Adsorption constant CO, bar^{-1}	T_{target}	Target outlet temperature, K
K_{CH_4}	Adsorption constant CH_4, bar^{-1}	ΔT_{app}	Approach temperature, K
$K_{eq,j}$	Equilibrium constant, —	ΔT_{min}	Minimum approach, K
K_{H_2}	Adsorption constant H_2, bar^{-1}	U	Heat transfer coefficient, W m^{-2} K^{-1}
u	Superficial velocity, m s^{-1}	W	Catalyst mass, kgcat

Greek symbols

ε_b Bed void fraction, —	ρ_b Bulk density, kg m^{-3}	ϕ_s Thiele modulus, —
μ_g Gas viscosity, Pa s	ρ_g Gas density, kg m^{-3}	τ_W Spatial time, kgcat s mol^{-1}
ν_{ji} Stoichiometric coefficient, —	ξ Axial position, —	

Subscripts and superscripts

0	Inlet condition	g	Gas phase	r	Reactor
app	Approach	i	Species index	sat	Saturation
b	Bulk	j	Reaction index	$steam$	Steam
BFW	Boiler feed water	k	Stage index	tot	Total
cat	Catalyst	L	Liquid	vap	Vaporisation
e	Effective	max	Maximum	W	Weight-based
eq	Equilibrium	min	Minimum	$^\circ$	Standard state

Annex

Table A1. Kinetic constants of the methanation model [51]

$k_{1,0}$	4.225×10^{15}	mol kg^{-1} s^{-1} bar$^{-2.5}$
Ea,1	240.1	kJ mol^{-1}

$k_{3,0}$	1.020×10^{15}	mol kg^{-1} s^{-1} bar^{-1}
Ea,3	67.13	kJ mol^{-1}
K_CO,0	8.23×10^{-5}	bar^{-1}
ΔHads,CO	−70.65	kJ mol^{-1}
$K\_H_2,0$	6.12×10^{-9}	bar^{-1}
$\Delta Hads,H_2$	−82.90	kJ mol^{-1}
$K\_CH_4,0$	6.65×10^{-4}	bar^{-1}
$\Delta Hads,CH_4$	−38.28	kJ mol^{-1}
$K\_H_2O,0$	1.77×10^{5}	adim.
$\Delta Hads,H_2O$	+88.68	kJ mol^{-1}

References

[1] Schmidt J, Gruber K, Klingler M, Klöckl C, Ramirez Camargo L, Regner P, et al. A new perspective on global renewable energy systems: why trade in energy carriers matters. Energy Environ Sci 2019;12:2022–9. https://doi.org/10.1039/C9EE00223E.

[2] Hosseini SE, Wahid MA. Hydrogen production from renewable and sustainable energy resources: Promising green energy carrier for clean development. Renewable and Sustainable Energy Reviews 2016;57:850–66. https://doi.org/10.1016/J.RSER.2015.12.112.

[3] Becker WL, Penev M, Braun RJ. Production of synthetic natural gas from carbon dioxide and renewably generated hydrogen: A techno-economic analysis of a power-to-gas strategy. Journal of Energy Resources Technology, Transactions of the ASME 2019;141. https://doi.org/10.1115/1.4041381/474624.

[4] Lee B, Lee H, Kang S, Lim H. Stochastic techno-economic analysis of power-to-gas technology for synthetic natural gas production based on renewable H2 cost and CO2 tax credit. J Energy Storage 2019;24:100791. https://doi.org/10.1016/J.EST.2019.100791.

[5] Schaaf T, Grünig J, Schuster MR, Rothenfluh T, Orth A. Methanation of CO2 - storage of renewable energy in a gas distribution system. Energy, Sustainability and Society 2014 4:1 2014;4:2-. https://doi.org/10.1186/S13705-014-0029-1.

[6] Rodriguez-Pastor DA, Garcia-Guzman A, Marqués-Valderrama I, Ortiz C, Carvajal E, Becerra JA, et al. A flexible methanol-to-methane thermochemical energy storage system (TCES) for gas turbine (GT) power production. Appl Energy 2024;356:122398. https://doi.org/10.1016/J.APENERGY.2023.122398.

[7] Brear MJ, Baldick R, Cronshaw I, Olofsson M. Sector coupling: Supporting decarbonisation of the global energy system. The Electricity Journal 2020;33:106832. https://doi.org/10.1016/J.TEJ.2020.106832.

[8] Detz R, Beerse M, Meulendijks N, Buskens P, van der Zwaan B. Towards the Use of Renewable Syngas for the Decarbonization of Industry. ChemSusChem 2024;17:e202400059. https://doi.org/10.1002/CSSC.202400059;SUBPAGE:STRING:FULL.

[9] Rauch R, Hrbek J, Hofbauer H. Biomass Gasification for Synthesis Gas Production and Applications of the Syngas. Advances in Bioenergy: The Sustainability Challenge 2015:73–91. https://doi.org/10.1002/9781118957844.CH7;PAGE:STRING:ARTICLE/CHAPTER.

[10] Daiyan R, Macgill I, Amal R. Opportunities and Challenges for Renewable Power-to-X. ACS Energy Lett 2020;5:3843–7. https://doi.org/10.1021/ACSENERGYLETT.0C02249.

[11] Gado MG, Al-Ghussain L, Alrbai M, Al-Dahidi S. Sustainable e-fuels production, liquefaction and transport technoeconomic feasibility using renewable energy resources. Energy Convers Manag 2025;345:120373. https://doi.org/10.1016/J.ENCONMAN.2025.120373.

[12] Menin L, Vakalis S, Benedetti V, Patuzzi F, Baratieri M. Techno-economic assessment of an integrated biomass gasification, electrolysis, and syngas biomethanation process. Biomass Conversion and Biorefinery 2020 11:2 2020;11:445–59. https://doi.org/10.1007/S13399-020-00654-9.

[13] Er-rbib H, Bouallou C. Modeling and simulation of CO methanation process for renewable electricity storage. Energy 2014;75:81–8. https://doi.org/10.1016/J.ENERGY.2014.05.115.

[14] Beniwal A, Bagaria A, Chen TY, Bhalothia D. Advancements in CO 2 conversion technologies: a comprehensive review on catalyst design strategies for high-performance CO 2 methanation. Sustain Energy Fuels 2025;9:2261–86. https://doi.org/10.1039/D5SE00167F.

[15] Rönsch S, Köchermann J, Schneider J, Matthischke S. Global Reaction Kinetics of CO and CO2 Methanation for Dynamic Process Modeling. Chem Eng Technol 2016;39:208–18. https://doi.org/10.1002/CEAT.201500327;WGROUP:STRING:PUBLICATION.

[16] Li C, Zhu X, Angelidaki I. Syngas biomethanation: effect of biomass-gas ratio, syngas composition and pH buffer. Bioresour Technol 2021;342:125997. https://doi.org/10.1016/J.BIORTECH.2021.125997.

[17] Hauser A, Weitzer M, Gunsch S, Neubert M, Karl J. Dynamic hydrogen-intensified methanation of synthetic by-product gases from steelworks. Fuel Processing Technology 2021;217:106701. https://doi.org/10.1016/J.FUPROC.2020.106701.
[18] Du J, Gao J, Gu F, Zhuang J, Lu B, Jia L, et al. A strategy to regenerate coked and sintered Ni/Al2O3 catalyst for methanation reaction. Int J Hydrogen Energy 2018;43:20661–70. https://doi.org/10.1016/J.IJHYDENE.2018.09.128.
[19] Li J, Zhou L, Li P, Zhu Q, Gao J, Gu F, et al. Enhanced fluidized bed methanation over a Ni/Al2O3 catalyst for production of synthetic natural gas. Chemical Engineering Journal 2013;219:183–9. https://doi.org/10.1016/J.CEJ.2013.01.005.
[20] Zhang Q, Guo X, Yao X, Cao Z, Sha Y, Chen B, et al. Modeling, simulation, and systematic analysis of high-temperature adiabatic fixed-bed process of CO methanation with novel catalysts. Appl Energy 2020;279:115822. https://doi.org/10.1016/J.APENERGY.2020.115822.
[21] Miao B, Kang S, Tong S, Hou S, Sai W, Pan Z, et al. Maximizing CH4 yield by thermodynamically optimizing the temperature profile of fixed-bed CO2 methanation reactors. Energy 360 2025;3:100018. https://doi.org/10.1016/J.ENERG.2025.100018.
[22] Gruber M, Weinbrecht P, Biffar L, Harth S, Trimis D, Brabandt J, et al. Power-to-Gas through thermal integration of high-temperature steam electrolysis and carbon dioxide methanation - Experimental results. Fuel Processing Technology 2018;181:61–74. https://doi.org/10.1016/J.FUPROC.2018.09.003.
[23] El Sibai A, Rihko Struckmann LK, Sundmacher K. Model-based Optimal Sabatier Reactor Design for Power-to-Gas Applications. Energy Technology 2017;5:911–21. https://doi.org/10.1002/ENTE.201600600;SUBPAGE:STRING:FULL.
[24] Flaischlen S, Martin J, Kreitz B, Turek T, Wehinger GD. Computational Fluid Dynamics Simulation of CO2 Methanation in a Fixed-bed Profile Reactor. Computer Aided Chemical Engineering 2020;48:499–504. https://doi.org/10.1016/B978-0-12-823377-1.50084-7.
[25] Sreedhar I, Varun Y, Singh SA, Venugopal A, Reddy BM. Developmental trends in CO2 methanation using various catalysts. Catal Sci Technol 2019;9:4478–504. https://doi.org/10.1039/C9CY01234F.
[26] Lee WJ, Li C, Prajitno H, Yoo J, Patel J, Yang Y, et al. Recent trend in thermal catalytic low temperature CO2 methanation: A critical review. Catal Today 2021;368:2–19. https://doi.org/10.1016/J.CATTOD.2020.02.017.
[27] Hatta AH, Jalil AA, Hassan NS, Hamid MYS, Bahari MB, Aziz MA, et al. A comprehensive review on the advancements in catalyst regeneration strategies for enhanced reactivity in CO methanation. Mater Today Chem 2023;33:101743. https://doi.org/10.1016/J.MTCHEM.2023.101743.
[28] Zyryanova MM, Snytnikov P V., Amosov YI, Kuzmin VA, Kirillov VA, Sobyanin VA. Design, scale-out, and operation of a preferential CO methanation reactor with a nickel–ceria catalyst. Chemical Engineering Journal 2011;176–177:106–13. https://doi.org/10.1016/J.CEJ.2011.03.085.
[29] Nguyen TTM, Wissing L, Skjøth-Rasmussen MS. High temperature methanation: Catalyst considerations. Catal Today 2013;215:233–8. https://doi.org/10.1016/J.CATTOD.2013.03.035.
[30] Muritala IK, Guban D, Roeb M, Sattler C. High temperature production of hydrogen: Assessment of non-renewable resources technologies and emerging trends. Int J Hydrogen Energy 2020;45:26022–35. https://doi.org/10.1016/J.IJHYDENE.2019.08.154.
[31] Fazlinezhad A, Yasari E. A novel dual-mode thermally coupled methanation reactor for sustainable power-to-gas: Multi-objective optimization and performance enhancement. Int J Hydrogen Energy 2026;203:153123. https://doi.org/10.1016/J.IJHYDENE.2025.153123.
[32] Engelbrecht N, Everson RC, Bessarabov D. Thermal management and methanation performance of a microchannel-based Sabatier reactor/heat exchanger utilising renewable hydrogen. Fuel Processing Technology 2020;208:106508. https://doi.org/10.1016/J.FUPROC.2020.106508.
[33] Schüler C, Wolf M, Hinrichsen O. Contactless temperature measurements under static and dynamic reaction conditions in a single-pass fixed bed reactor for CO2 methanation. Journal of CO2 Utilization 2018;25:158–69. https://doi.org/10.1016/J.JCOU.2018.03.016.
[34] Rostrup-Nielsen JR, Pedersen K, Sehested J. High temperature methanation: Sintering and structure sensitivity. Appl Catal A Gen 2007;330:134–8. https://doi.org/10.1016/J.APCATA.2007.07.015.
[35] Krammer A, Medved A, Peham M, Wolf-Zöllner P, Salbrechter K, Lehner M. Dual Pressure Level Methanation of Co-SOEC Syngas. Energy Technology 2021;9:2000746. https://doi.org/10.1002/ENTE.202000746;WEBSITE:WEBSITE:PERICLES;ISSUE:ISSUE:DOI.
[36] Lehner M, Tichler R, Steinmüller H, Koppe M. Methanation 2014:41–61. https://doi.org/10.1007/978-3-319-03995-4_4.
[37] Burkhardt M, Busch G. Methanation of hydrogen and carbon dioxide. Appl Energy 2013;111:74–9. https://doi.org/10.1016/J.APENERGY.2013.04.080.
[38] Laprune D, Farrusseng D, Schuurman Y, Meunier FC, Pieterse JAZ, Steele AM, et al. Effects of H2S and phenanthrene on the activity of Ni and Rh-based catalysts for the reforming of a simulated biomass-derived producer gas. Appl Catal B 2018;221:206–14. https://doi.org/10.1016/J.APCATB.2017.09.015.

[39] Jiang L, Hu S, Wang Y, Su S, Sun L, Xu B, et al. Catalytic effects of inherent alkali and alkaline earth metallic species on steam gasification of biomass. Int J Hydrogen Energy 2015;40:15460–9. https://doi.org/10.1016/J.IJHYDENE.2015.08.111.
[40] Nguyen P. Dynamic modelling and simulation of catalytic carbon dioxide methanation with green hydrogen 2024.
[41] Gao J, Jia C, Li J, Zhang M, Gu F, Xu G, et al. Ni/Al2O3 catalysts for CO methanation: Effect of Al2O3 supports calcined at different temperatures. Journal of Energy Chemistry 2013;22:919–27. https://doi.org/10.1016/S2095-4956(14)60273-4.
[42] Mihet M, Lazar MD. Methanation of CO2 on Ni/γ-Al2O3: Influence of Pt, Pd or Rh promotion. Catal Today 2018;306:294–9. https://doi.org/10.1016/J.CATTOD.2016.12.001.
[43] Song H, Yang J, Zhao J, Chou L. Methanation of Carbon Dioxide over a Highly Dispersed Ni/La2O3 Catalyst. Chinese Journal of Catalysis 2010;31:21–3. https://doi.org/10.1016/S1872-2067(09)60036-X.
[44] Alrafei B, Polaert I, Ledoux A, Azzolina-Jury F. Remarkably stable and efficient Ni and Ni-Co catalysts for CO2 methanation. Catal Today 2020;346:23–33. https://doi.org/10.1016/J.CATTOD.2019.03.026.
[45] Hu CW, Yao J, Yang HQ, Chen Y, Tian AM. On the Inhomogeneity of Low Nickel Loading Methanation Catalyst. J Catal 1997;166:1–7. https://doi.org/10.1006/JCAT.1997.1469.
[46] Tsiotsias AI, Charisiou ND, Yentekakis I V., Goula MA. The Role of Alkali and Alkaline Earth Metals in the CO2 Methanation Reaction and the Combined Capture and Methanation of CO2. Catalysts 2020, Vol 10, Page 812 2020;10:812. https://doi.org/10.3390/CATAL10070812.
[47] Hu D, Gao J, Ping Y, Jia L, Gunawan P, Zhong Z, et al. Enhanced Investigation of CO Methanation over Ni/Al2O3 Catalysts for Synthetic Natural Gas Production. Ind Eng Chem Res 2012;51:4875–86. https://doi.org/10.1021/IE300049F.
[48] Liu K, Nawaz MA, Liao G. Progress and Future Challenges in Designing High-Performance Ni/CeO2 Catalysts for CO2 Methanation: A Critical Review. Carbon Neutralization 2025;4:e190. https://doi.org/10.1002/CNL2.190;WEBSITE:WEBSITE:PERICLES;REQUESTEDJOURNAL:JOURNAL:27693325;WGROUP:STRING:PUBLICATION.
[49] Luisetto I, Tuti S, Battocchio C, Lo Mastro S, Sodo A. Ni/CeO2–Al2O3 catalysts for the dry reforming of methane: The effect of CeAlO3 content and nickel crystallite size on catalytic activity and coke resistance. Appl Catal A Gen 2015;500:12–22. https://doi.org/10.1016/J.APCATA.2015.05.004.
[50] Tiwari S, Arghode V, Deo G. Synthesis and enhanced performance of Ni–Co/Al2O3 washcoated Ni foam for flue-gas reforming of methane. Int J Hydrogen Energy 2026;229:154771. https://doi.org/10.1016/J.IJHYDENE.2026.154771.
[51] Xu J, Froment GF. Methane steam reforming, methanation and water-gas shift: I. Intrinsic kinetics. AIChE Journal 1989;35:88–96. https://doi.org/10.1002/AIC.690350109;WEBSITE:WEBSITE:AICHE;ISSUE:ISSUE:DOI.
[52] Hu D, Gao J, Ping Y, Jia L, Gunawan P, Zhong Z, et al. Enhanced Investigation of CO Methanation over Ni/Al2O3 Catalysts for Synthetic Natural Gas Production. Ind Eng Chem Res 2012;51:4875–86. https://doi.org/10.1021/IE300049F.
[53] Medina OE, Amell AA, López D, Santamaría A. Comprehensive review of nickel-based catalysts advancements for CO2 methanation. Renewable and Sustainable Energy Reviews 2025;207:114926. https://doi.org/10.1016/J.RSER.2024.114926.
[54] Schlereth D, Hinrichsen O. A fixed-bed reactor modeling study on the methanation of CO2. Chemical Engineering Research and Design 2014;92:702–12. https://doi.org/10.1016/J.CHERD.2013.11.014.
[55] Haldor Topsoe. From solid fuels to substitute natural gas (SNG) using TREMP™ Topsøe Recycle Energy-efficient Methanation Process 2009.
[56] Xu J, Froment GF. Methane steam reforming: II. Diffusional limitations and reactor simulation. AIChE Journal 1989;35:97–103. https://doi.org/10.1002/AIC.690350110;JOURNAL:JOURNAL:15475905;PAGEGROUP:STRING:PUBLICATION.
[57] Chase M. NIST-JANAF thermochemical tables 1998.
[58] Rodriguez-Pastor DA, Carro A, Masci G, Ortiz C, Verda V, Chacartegui R. Conceptualizing novel CH3OH-based thermochemical energy storage routes via a modeling approach. Cell Rep Phys Sci 2023;0:101357. https://doi.org/10.1016/J.XCRP.2023.101357.
[59] Ali El Sibai von, Kai Sundmacher Dr-Ing Christof Hamel Liisa Rihko-Struckmann D-I. Model-based optimization and experimental investigation of CO2 methanation 2019. https://doi.org/10.25673/32608.
[60] Bremer J, Sundmacher K. Operation range extension via hot-spot control for catalytic CO2 methanation reactors. React Chem Eng 2019;4:1019–37. https://doi.org/10.1039/C9RE00147F.
[61] Giglio E, Deorsola FA, Gruber M, Harth SR, Morosanu EA, Trimis D, et al. Power-to-Gas through High Temperature Electrolysis and Carbon Dioxide Methanation: Reactor Design and Process Modeling. Ind Eng Chem Res 2018;57:4007–18. https://doi.org/10.1021/ACS.IECR.8B00477.